JOURNAL OF GEOPHYSICAL RESEARCH, VOL. 101, NO. D5, PAGES 9333-9343, APRIL 27, 1996

Interpretation of TOVS water vapor radiances in terms of layer-average relative humidities: Method and climatology for the upper, middle, and lower troposphere

Brian J. Soden

Geophysical Fluid Dynamics Laboratory, NOAA, Princeton, New Jersey

Francis P. Bretherton

Space Science and Engineering Center, University of Wisconsin-Madison

Abstract. This study presents an analytical expression, derived from radiative theory, for relating water vapor radiances to layer-average relative humidities. This "radiance-to-humidity transformation" provides a simple, yet reliable, means of interpreting satellite observations of the upwelling radiation in the 6.3-μm water vapor absorption band in terms of a more familiar water vapor quantity. Despite its simplicity, when compared to detailed radiative transfer calculations of the upper (6.7 μm) tropospheric water vapor radiance, the transformation is demonstrated to be accurate to within ~1 K. Similar levels of accuracy are found when the transformation is compared to detailed calculations of the middle (7.3 μm) and lower (8.3 μm) tropospheric water vapor radiance, provided that the emission from the underlying surface is taken into account. On the basis of these results, the radiance-to-humidity transformation is used to interpret TIROS operational vertical sounder observed water vapor radiances in terms of the relative humidity averaged over deep layers of the upper, middle, and lower troposphere. We then present near-global maps of the geographic distribution and climatological variations of upper, middle, and lower-tropospheric humidity for the period 1981-1991. These maps clearly depict the role of the large-scale circulation in regulating the location and temporal variation of tropospheric water vapor.

1. Introduction

Water vapor plays a fundamental role in regulating the Earth's climate both directly through its effect on the radiation balance and indirectly through its coupling with other components of the hydrologic cycle. Yet despite its importance, significant gaps in our knowledge of atmospheric moisture still exist. One source of information on tropospheric water vapor which has not been sufficiently utilized for climate studies is water vapor radiances measured by the TIROS operational vertical sounder (TOVS). The TOVS instrument package provides measurements of the upwelling radiance in a range of spectral channels, three of which are located within the 6.3-μm water vapor absorption band. These channels, located at 6.7 μm, 7.3 μm, and 8.3 μm, are sensitive to the amount of water vapor integrated over broad layers centered in the upper (200-500 mbar), middle (300-700 mbar), and lower troposphere (600 mbar - surface), respectively (see Figure 1).

Two aspects of the TOVS water vapor radiances make them well suited for climatological studies: (1) High spatial and temporal coverage, the TOVS instrument is carried onboard the National Oceanic and Atmospheric Administration series of polar orbiting satellites which provide near global coverage every 12 hours, and (2) the availability of a lengthy data set, a temporally coherent archive of TOVS water vapor radiances exists from February 1979 to present, providing an invaluable time series for describing the distribution and variation of moisture on time scales from days to years. This combination of high spatial/temporal coverage and lengthy duration is unmatched by any other water vapor archive.

However, there are some limitations to the TOVS water vapor radiance data set. Since the measurements are sensitive to the integrated amount of moisture over layers several kilometers thick, TOVS radiances provide only limited information on the vertical distribution of moisture. While this has long been a problem for assimilating the information into numerical models, it is less of a hindrance for climatological studies which are often interested in the characteristics of moisture averaged over a finite depth of the atmosphere rather than at a single level. Another limitation is that, owing to the strong attenuation of infrared radiation by clouds, most information on water vapor is negated when clouds obscure the region of interest. Fortunately, the impact of this problem is ameliorated by the relatively high horizontal resolution of the TOVS water vapor channels (~20 km at nadir). For example, using the N* cloud-clearance technique [*McMillin and Dean*, 1982] estimates of the clear-sky radiance averaged over a roughly 200 km x 100 km region are obtained in conditions of up to 75% cloud cover. Nevertheless, since cloud cover is correlated with relative humidity, the restriction to clear and partially cloudy conditions is likely to introduce a sampling bias. In an attempt to quantify this bias, *Soden and Lanzante* [1996] compared a total-sky radiosonde climatology of relative humidity with the

Paper number 96JD00280.
0148-0227/96/96JD-00280$05.00

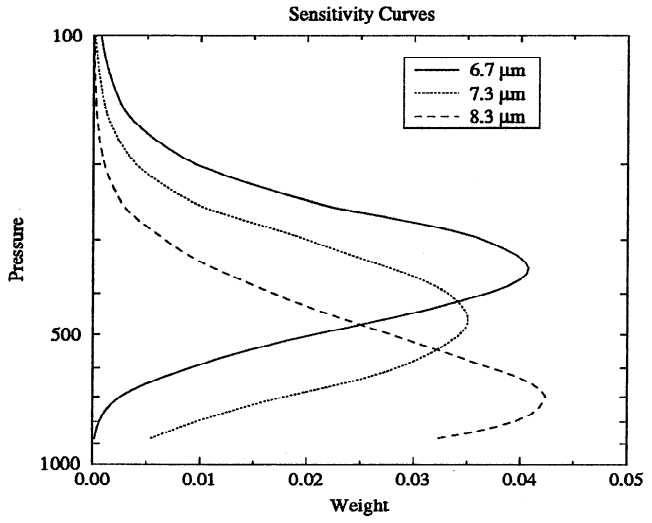

Figure 1. Sensitivity of $T_{6.7}$ (solid), $T_{7.3}$ (dotted), and $T_{8.3}$ (dashed) to local perturbations in relative humidity in thin layers equally spaced in the logarithm of pressure ($\Delta \ln p = dp/p \cong 0.04$). The curves are normalized such that the sum of weights over pressure is equal to unity.

corresponding clear-sky radiosonde climatology containing the identical sampling restrictions present in the satellite data. This study suggested that the restriction to clear and partially cloudy conditions introduces a slight dry bias into the TOVS climatology, typically about 4% and usually less than 10% when expressed in terms of the relative humidity. We note, however, that these results were heavily weighted toward the northern hemisphere midlatitudes and hence may not be representative of all regions.

Despite the availability of extensive archives of TOVS water vapor radiances, only recently have they begun to be used for climate studies [*Wu et al.*, 1993; *Salathe et al.*, 1995; *Soden and Fu*, 1995; *Bates et al.*, 1996, *Soden and Lanzante*, 1996]. One reason for the lack of attention is due to the difficulty of interpreting the observed radiances in terms of a more familiar water vapor quantity. In their study of the GOES 6.7-μm channel, *Soden and Bretherton* [1993] (hereafter referred to as SB93) addressed this issue by deriving an analytic expression, based upon simplified radiative theory, to relate water vapor radiances to relative humidity. Rather than attempting retrievals in the form of vertical soundings, attention was focused on the information actually present in the observations, minimizing extraneous assumptions. This analytical relationship, hereafter called a radiance-to-humidity transformation, is summarized in section 2 and provides a convenient means of interpreting the radiances in terms of a more familiar water vapor quantity, namely a layer-average relative humidity.

The purposes of this paper are (1) to demonstrate the radiance-to-humidity transformation using TOVS upper tropospheric water vapor radiances (6.7 μm), (2) to extend the radiance-to-humidity transformation to the middle (7.3 μm) and lower (8.3 μm) tropospheric water vapor radiances by including an allowance for the surface emission, (3) to examine the sensitivity of the inferred moisture distribution to the empirical tuning of the transformation, and (4) to present near-global maps of the upper, middle, and lower tropospheric relative humidity inferred from TOVS using the radiance-to-humidity transformation and explore their seasonal and interannual variations. The remaining portion of this paper is organized as follows: Section 2 briefly reviews the derivation of the radiance-to-humidity transformation developed by SB93. Section 3 demonstrates the consistency of the transformation with detailed calculations of the upper, middle, and lower tropospheric water vapor radiances and presents a sensitivity analysis of the procedure. Section 4 displays maps of the climatological variations of upper, middle, and lower tropospheric humidity inferred from TOVS, and the conclusions of this study are summarized in section 5.

2. Radiance-to-Humidity Transformation

This section summarizes aspects of the radiance-to-humidity transformation relevant to the present study, the reader is referred to SB93 for a complete derivation. To facilitate the interpretation of satellite-observed water vapor radiances, SB93 developed a simplified model of radiative transfer based upon a set of strongly absorbing, pressure-broadened lines. Following *Goody* [1964], each narrow, irregularly spaced line is assumed to behave as an independent isolated absorber, and the assemblage is then modeled as a large number of randomly located, overlapping lines. Using this random strong line theory and considering an idealized atmospheric profile in which the relative humidity r and dimensionless lapse rate $\beta = p/T\, dT/dp$ are constant over the range of pressures to which the water vapor channel is sensitive, a simple analytical expression for the brightness temperature (T_b) may be obtained (see (20) of SB93)

$$a + bT_b = \log_e\left(\frac{rp_o}{\beta \cos\theta}\right) \qquad (1)$$

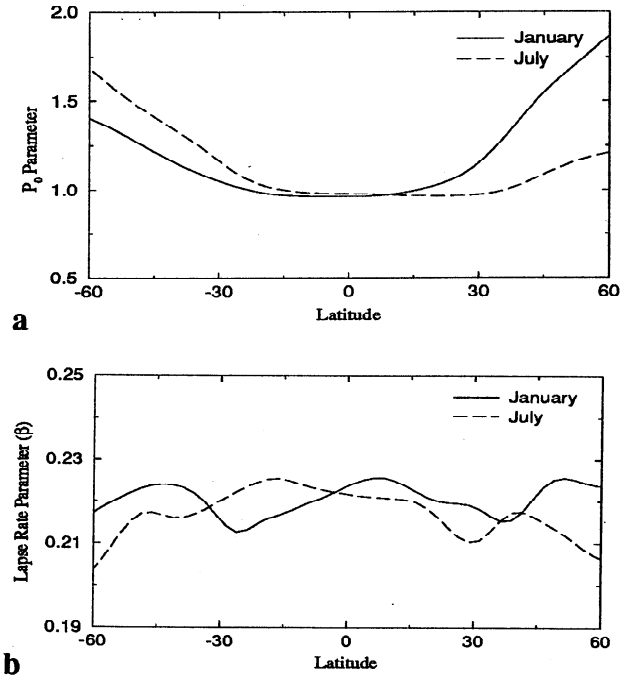

Figure 2. Zonal mean distribution of (a) normalized base pressure $p_o = p(T = 240\ \text{K})/300$ mbar and (b) normalized lapse rate $\beta = p/T\, dT/dp$ for January and July determined from a 4-year climatology of European Centre for Medium-Range Weather Forecasts analyses.

The variables comprising the right-hand side of (1) are the relative humidity r, lapse rate β, satellite zenith angle θ, and a reference pressure p_o which is equal to the pressure of the 240 K isotherm divided by 300 mbar ($p_o = p[T = 240\ K]/300$ mbar). This expression, which is the central result of the radiance-to-humidity transformation derived by SB93, provides a simple means of interpreting the brightness temperature in terms of more familiar atmospheric quantities. It demonstrates that for a profile with constant relative humidity and lapse rate, the brightness temperature varies logarithmically with the ratio ($rp_o/\beta\cos\theta$). Changes in relative humidity represent the largest source of variation in brightness temperature with a factor of 2 increase in r resulting in a decrease in T_b of $\log(2)/b \cong 6$ K. The normalized base pressure p_o varies between the tropics ($p_o \cong 0.9$) and midlatitudes ($p_o \cong 1.5$) by +/- 25% and thus also constitutes an important source of variation in T_b. Fortunately, p_o varies in a quite predictable manner. Figure 2a shows the zonally average distribution of p_o for January and July as determined from European Centre for Medium-Range Weather Forecasts (ECMWF) analyses. Figure 2a illustrates that the dominant sources of variation in p_o reflect the seasonal and latitudinal shifts in the mean temperature structure of the troposphere. These variations are easily determined from temperature climatologies (e.g., operational analyses) and thus their impact upon the T_b can be readily accounted for. The relative variations in atmospheric lapse rate are roughly +/- 5% ($\beta \cong 0.21$ +/-.01) or roughly a factor of five smaller than variations in p_o and exhibit a less systematic geographic distribution (figure 2b); consequently, they are of less importance for interpreting the water vapor radiances. Thus to a reasonable degree of accuracy (+/- 0.5 K) variations in β may be neglected, and a modified form of (1) can be used,

$$a + bT_b = \log_e\left(\frac{rp_o}{\cos\theta}\right) \qquad (2)$$

This simplified form of the radiance-to-humidity transformation predicts that the water vapor T_b measures essentially the logarithm of the mean relative humidity averaged over broad layers of the troposphere subject to a straight forward allowance for viewing angle ($\cos\theta$) and a minor correction for the mean temperature structure (p_o). We also note that throughout this paper the relative humidity r is defined to be with respect to water. Although the relative humidity with respect to ice may be more appropriate for the subfreezing temperatures in the upper troposphere, the relative humidity with respect to water is chosen to provide a parameter which is consistent between all three channels (e.g., the upper, middle, and lower troposphere).

This form of (2) differs slightly from that used by SB93 for the GOES 6.7-μm channel (see (23) of SB93). Namely, SB93 did not include variations in p_o in their final relationship (although its importance was expected), noting that it did not significantly improve the agreement with radiative transfer calculations. The reason for this was not well understood by SB93 but now is believed to be a spurious result related to the GOES viewing geometry. Since the GOES platform is geostationary, higher latitudes are viewed with a systematically larger zenith angle, particularly for middle to high latitudes. As a result, the layer which the GOES $T_{6.7}$ senses shifts toward higher levels of the upper troposphere. This effect was accounted for in computing the radiances but not in determining the layer-average relative humidity. Since relative humidity within the upper troposphere typically decreases with height, high zenith angle measurements (e.g., over the midlatitudes) sense lower relative humidities, and this effect acts to compensate for the increase in p_o with latitude. Thus for GOES, the expected variations in p_o were masked by the systematic variations in viewing angle with latitude combined with a decrease in relative humidity with height in the upper troposphere.

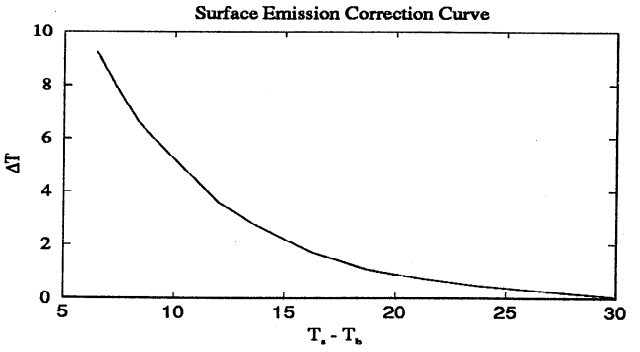

Figure 3. Brightness temperature correction (ΔT) as a function of the difference between the surface temperature (T_s) and observed brightness temperature (T_b) [after *Soden and Bretherton*, 1993].

In deriving (2) it is also assumed that the atmosphere is sufficiently opaque such that the surface contribution to the observed T_b is negligible. While this assumption is generally valid for the upper tropospheric water vapor channel (6.7 μm) for which (2) was originally derived, it is not always true for the middle (7.3 μm) and lower (8.3 μm) tropospheric water vapor channels. In situations where the surface emission is an important component of the observed T_b, it is necessary to adjust the T_b to account for the surface contribution. This surface adjustment is analogous to the procedure described by SB93 to account for the radiance contribution of underlying clouds in the 6.7-μm channel (see section 4.3 of SB93 for details). Figure 3 shows the brightness temperature correction ΔT as a function of the difference between the surface temperature T_s and the brightness temperature T_b. When the T_b is at least 20 K cooler than T_s, the surface contribution is negligible and no correction is necessary. For the latitudes of interest in this study (60°N-60°S), this is virtually always the case for the upper tropospheric channel and is the norm for the middle tropospheric channel. The lower tropospheric channel, on the other hand, is rarely 20 K cooler than T_s, and hence a correction is almost always necessary. At the other extreme, when the difference between the T_s and T_b is only 7 K, the surface correction is also 7 K. That is, the correction ΔT is now as large as the signal from the water vapor above the surface, and this is roughly the upper limit for which a T_b correction is reasonable.

3. Comparison With Radiative Transfer Calculations

In this section, we investigate the validity of the radiance-to-humidity transformation by comparing the simple logarithmic relationship predicted by (2) with detailed radiative transfer calculations.

3.1. Upper Tropospheric Water Vapor Radiances

The 6.7-μm channel is located near the center of the 6.3-μm water vapor absorption band and under clear-sky conditions is sensitive primarily to the relative humidity averaged over a broad layer centered in the upper troposphere (roughly 200-500 mbar). Figure 1 illustrates the sensitivity of the 6.7-μm channel to perturbations in relative humidity for a typical tropical profile viewed at zenith.

Equation (2) predicts that the brightness temperature at 6.7 μm ($T_{6.7}$) should vary logarithmically with the ratio $\bar{r}_u p_o/\cos\theta$, where $\bar{r}_u$ represents the vertically averaged relative humidity in the upper troposphere weighted according to the 6.7-μm sensitivity curve (e.g., Figure 1) and sum to unity. The actual weighting profile varies slightly depending upon the precise nature of the temperature and moisture profile, being slightly higher for warm tropical profiles and slightly lower for cold, midlatitude winter profiles. Thus when plotted as a function of pressure, the weighting profile will shift depending primarily upon the temperature structure of the atmosphere (see Table 2 of SB93). However, when temperature is used as the vertical coordinate, the position of the weighting profile remains relatively unchanged when moving from the tropics to midlatitudes. Thus to a reasonable approximation, a single set of temperature-dependent weights may be used for all profiles, irrespective of the precise nature of the profile. Table 1 lists the weights for computing $\bar{r}_u$ from a relative humidity profile provided on 10 K isotherms. Interpolation between isotherms is appropriate, provided the weights are normalized to unity.

To evaluate the validity of the radiance-to-humidity transformation, we compare the relationship predicted in (2) with detailed calculations of the 6.7-μm radiance using the RTTOVS model [*Eyre*, 1991]. Figure 4a compares synthetic $T_{6.7}$ calculated from a sample profile data set versus the corresponding value of $\log(\bar{r}_u p_o/\cos\theta)$, where $\bar{r}_u$ is calculated explicitly from the same set of atmospheric profiles using weights from Table 1; p_o is obtained as a function of month, latitude, and longitude using a 4-year ECMWF climatology and $\cos\theta = 1$. To provide a sample representative of a wide range of atmospheric conditions, the temperature and moisture profiles are obtained from ECMWF operational analyses for July 1, 1988 using all profiles (~8000) equatorward of 60° latitude. A zenith viewing geometry ($\cos\theta = 1$) is chosen for all calculations to be consistent with the TOVS limb-corrected radiances examined in section 4. (In generating the TOVS archive, the National Environmental Satellite Data and Information Service (NESDIS) applies a limb correction to convert the TOVS radiances viewed at a variety of zenith angles to equivalent nadir-view radiances ($\theta = 0$). This procedure serves to remove the impact of varying viewing geometry upon the TOVS radiance field.)

Table 1. Weights for Determining $\bar{r}$

Temperature Level, K	Weights $\bar{r}_u$	$\bar{r}_m$	$\bar{r}_l$
220	0.06	0.03	0.01
230	0.14	0.06	0.02
240	0.23	0.12	0.04
250	0.25	0.18	0.08
260	0.20	0.22	0.14
270	0.09	0.21	0.22
280	0.03	0.14	0.28
290	0.00	0.04	0.21

Weights w_i for estimating $\bar{r}$ from a profile of relative humidity r_i provided on equally spaced temperature levels i; that is, $\bar{r} = (\sum r_i w_i)/(\sum w_i)$ for all temperature levels occurring within the sounding. Subscripts u, m, and l denote upper, middle, and lower, respectively.

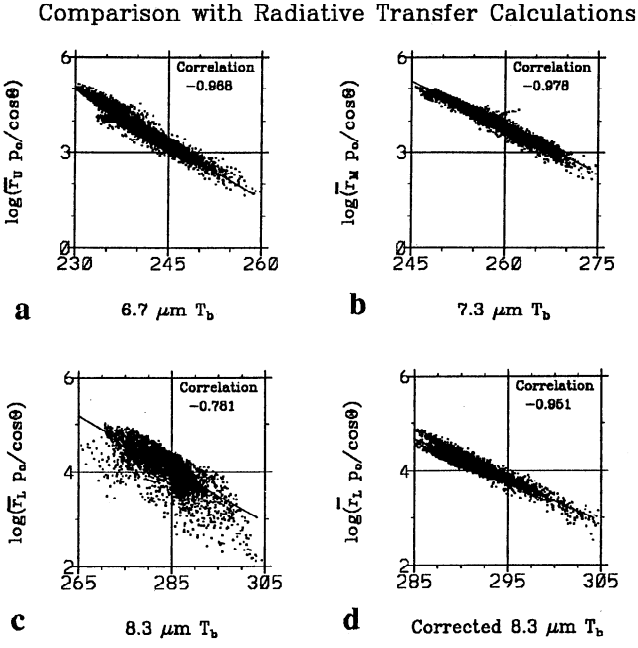

Figure 4. Scatter plot of synthetic radiance calculations versus logarithmic relationship predicted from (2). (a) $T_{6.7}$ versus $\log(\bar{r}_u p_o/\cos\theta)$, (b) $T_{7.3}$ versus $\log(\bar{r}_m p_o/\cos\theta)$, (c) $T_{8.3}$ versus $\log(\bar{r}_l p_o/\cos\theta)$, (d) $T^*_{8.3}$ (corrected for surface emission) versus $\log(\bar{r}_m p_o/\cos\theta)$. The solid line represents a least-squares fit used to determine the coefficients (a,b) in (2).

Equation (2) predicts that $T_{6.7}$ should be a linear function of $\log(\bar{r}_u p_o/\cos\theta)$. The detailed radiance calculations support this prediction, revealing a very strong linear correlation (-0.98) between the forward calculations of $T_{6.7}$ and the corresponding value of $\log(\bar{r}_u p_o/\cos\theta)$. Thus the simple radiance-to-humidity relationship explains greater than 90% of the variability in $T_{6.7}$. The correlation is negative indicating that as the relative humidity increases, the $T_{6.7}$ decreases.

The good agreement of the radiance calculations with (2) supports the validity of the simple relationship and demonstrates that, to a reasonable degree of accuracy, measurements of $T_{6.7}$ can be interpreted in terms of the relative humidity vertically-averaged over a range of pressure in the upper troposphere. On the basis of these results, (2) can be used to interpret the TOVS-observed $T_{6.7}$ in terms of a vertically averaged upper tropospheric relative humidity (UTH) according to

$$\mathrm{UTH} = \frac{\cos\theta}{p_o} e^{(31.5 - 0.115\, T_{6.7})} \qquad (3)$$

where the slope and intercept coefficients for (2) (a = 31.5 and b = -0.115 K^{-1}) are determined from a linear fit of the data in

Figure 4a and are consistent with the theoretically expected values (see SB93). The scatter in $T_{6.7}$ in Figure 4a is ~1.1 K which corresponds to an uncertainty of $\Delta \log_e(\mathrm{UTH}) \approx \Delta \mathrm{UTH}/\mathrm{UTH} \approx b\Delta T_{6.7} \approx 0.13$ in UTH. If we consider a UTH of 50%, then a rough estimate of the uncertainty due to the scatter in Figure 4a, expressed in terms of relative humidity, is (0.13)(50%) = 6.5%.

3.2. Middle Tropospheric Water Vapor Radiances

The sensitivity of the 7.3-μm brightness temperature ($T_{7.3}$) to variations in relative humidity for a typical tropical profile is shown in Figure 1. Since the atmospheric attenuation is smaller at 7.3 μm than at 6.7 μm, the $T_{7.3}$ is sensitive to relative humidity averaged over a slightly lower layer of atmosphere (roughly 300 to 700 mbar). Although this channel is located farther away from the center of the 6.3-μm band, the basic assumptions used in deriving (2) are still valid, namely, that water vapor is the principal absorber (i.e., absorption by other constituents can be neglected [*Poc et al.*, 1981]) and that the absorption can be modeled as a series of randomly overlapped, strongly absorbing, pressure-broadened lines. Hence (2) should also be valid for $T_{7.3}$, provided that the vertically averaged relative humidity $\bar{r}_m$ is now determined using weights for the middle tropospheric channel (listed in Table 1).

The consistency between (2) and the radiative transfer calculations is illustrated in Figure 4b which compares synthetically calculated $T_{7.3}$ with the corresponding value of $\log(\bar{r}_m p_o/\cos\theta)$. The radiance calculations for the 7.3-μm water vapor channel exhibit good agreement with the radiance-to-humidity transformation (-0.98), demonstrating that (2) is also applicable for interpreting the $T_{7.3}$ in terms of a vertically averaged middle tropospheric relative humidity. The regression coefficients determined from a linear fit of the data are a = 28.7 b = -0.096 K^{-1} and the scatter in $T_{7.3}$ for a given value of $\bar{r}_m$ is +/- 1.0 K, consistent with that obtained for the 6.7 μm channel. Based upon these results, a transformation similar to (3) can be derived for interpreting radiances from the 7.3 μm channel in terms of a middle-tropospheric relative humidity (MTH)

$$\mathrm{MTH} = \frac{\cos\theta}{p_o} e^{(28.7 - 0.096\, T^*_{7.3})} \qquad (4)$$

For the July simulations described above, virtually all the $T_{7.3}$ are at least 20 K colder than the surface temperature, and therefore no surface correction is required. However, this is not the case year-round. During boreal winter, the atmosphere over the continental interiors of the northern midlatitudes becomes relatively transparent owing to the cold, dry conditions, and correction for the surface contribution becomes necessary. Rather than demonstrate this procedure here, an illustration of the surface correction and its importance is provided in section 3.3 for the lower tropospheric channel, where its impact is most evident.

3.3. Lower Tropospheric Water Vapor Radiances

The 8.3-μm channel is located furthest from the center of the 6.3-μm band and therefore senses deepest into the atmosphere of the three water vapor channels. The sensitivity of $T_{8.3}$ to variations in relative humidity (Figure 1) demonstrates that the $T_{8.3}$ are primarily influenced by the relative humidity below ~600 mbar. Since the atmosphere is more transparent at 8.3 μm, the impact of the surface contribution is also greatest for this channel. The importance of this effect is demonstrated in Figure 4c which compares the forward calculated $T_{8.3}$ (with no surface correction) versus $\log(\bar{r}_l p_o/\cos\theta)$, where $\bar{r}_l$ is calculated using the lower tropospheric weighting curves listed in Table 1. As suspected, a relatively poor correlation is evident (-0.73) indicating that the radiance-to-humidity transformation can only explain ~50% of the variations in the $T_{8.3}$. This scatter is attributable to the large surface contribution for this particular channel. However, if the temperature of the surface is known, its contribution to the upwelling $T_{8.3}$ at the top-of-the-atmosphere can be readily accounted for as described in section 2. To demonstrate this, the simulated $T_{8.3}$ from Figure 4c are adjusted to account for the surface contribution using the correction curve from Figure 3 and the surface temperature corresponding to each of the input profiles. The results are shown in Figure 4d. Accounting for the surface contribution significantly improves the agreement between the radiative transfer calculations and the radiance-to-humidity transformation (-0.95). The relationship predicted by (2) now explains greater than 90% of the variation in brightness temperature, and the scatter is reduced from > 5 K to ~1 K.

This comparison illustrates two points: (1) surface emission, in addition to lower tropospheric moisture, is an important variable in determining the $T_{8.3}$ field, and (2) when the surface contribution is accounted for, detailed calculations of $T_{8.3}$ agree well with the simple relationship predicted by (2). Using these results, a lower tropospheric relative humidity (LTH), which corresponds to a relative humidity averaged over a layer extending from roughly 600 mbar to the surface, can be inferred from the TOVS surface-corrected 8.3-μm brightness temperature climatology ($T^*_{8.3}$) according to

$$\mathrm{LTH} = \frac{\cos\theta}{p_o} e^{(29.8 - 0.088\, T^*_{8.3})} \qquad (5)$$

3.4. Sensitivity Analysis

In sections 3.1 to 3.3, the coefficients for (2) were determined for each channel by comparing synthetic radiances calculated from representative profiles of temperature and moisture with the corresponding vertically averaged relative humidity from the same profiles. To determine these coefficients, ECMWF analyses were used to provide the sample profiles. Hence this procedure essentially represents a tuning of (2) to the RTTOVS calculations for each channel, using ECMWF analyses to provide the sample temperature and moisture profiles. Here we demonstrate that the relative humidity parameters are insensitive to the sample profile data set used in deriving the coefficients for (2). For brevity, results are only shown for the upper tropospheric channel, since a sensitivity analysis for the middle and lower tropospheric channels leads to similar conclusions.

To examine the sensitivity of the humidity parameters to the tuning procedure, we compare the UTH determined with the coefficients from (3) (hereafter referred to as the "reference" UTH) with that determined using two new pairs of coefficients, each derived using a different sample profile data set: (1) the National Meteorological Center analyses (NMC) and (2) the TOVS initial guess retrieval (TIGR) radiosonde profiles. The NMC data set consists of a collection

Table 2. Sensitivity Analysis of UTH

Profile Set	*a*	*b*	Correlation	rms, %	Bias, %
TIGR	31.7	-0.116	0.999	2.9	2.6
NMC	35.5	-0.132	0.998	3.8	1.9
Reference	31.5	-0.115	1.000	0.0	0.0

The sensitivity of upper tropospheric relative humidity (UTH) to the sample profile data set. The correlation, rms difference, and bias are calculated with respect to the reference UTH. NMC, National Meteorological Center; TIGR, TOVS initial guess retrieval.

of roughly 8000 profiles taken from the operational analysis produced for December 1, 1989, using all profiles equatorward of 60° latitude. The TIGR profile data set is a collection of roughly 1700 soundings carefully selected from a much larger data set (~100,000) with the objective that they should be representative of the global atmosphere at any time and place [*Monine et al.*, 1987]. Table 2 lists the coefficients obtained from both new profile data sets. Figure 5 compares the annual mean climatology of the reference UTH with that obtained from both pairs of new coefficients, where each data point corresponds to the UTH from a 2.5° grid box between 60°N and 60°S. Statistics from this comparison are listed in Table 2.

There are two points to be made with this analysis. (1) Spatial variations in the relative humidity indices are not dependent upon the particular set of coefficients used but rather are a reflection of variations in the water vapor radiance field. This is evidenced by the near-perfect correlation (>0.99) between the reference UTH and that determined using either of the new coefficients. (2) Although systematic biases result when different coefficients are used, these differences are small (less than 5%). Thus, although the precise value of the humidity inferred from the TOVS radiances can depend upon the profile data set used to tune (2), the uncertainty is small relative to the magnitude of the regional and temporal variations of relative humidity.

In essence, (2) provides a simple analytical relation derived from radiative transfer theory, tuned to agree with the RTTOVS calculations, and is insensitive to the particular profile data set used in the tuning. This insensitivity reflects both a certain degree of consistency between the various profile data sets as well as the fundamental nature of the physical principles upon which equation (2) is based. It should be noted, however, that systematic differences of up to 2 K have been found between various radiative transfer models used for the 6.7 μm channel [*Murty et al.*, 1993; *Salathe and Smith*, 1996; *Soden and Lanzante*, 1996]. Hence tuning (2) using different radiative transfer models can lead to systematic differences in the derived UTH. Given the importance of forward radiance calculations in any retrieval, further work is clearly needed to fully assess the accuracy of transmittance models for the 6.3-μm band.

4. Climatologies of Upper, Middle, and Lower Tropospheric Humidity

This section presents near-global maps of the annual-mean distribution, seasonal variation, and interannual variation of relative humidity in the upper, middle, and lower troposphere derived from the TOVS water vapor radiances. For a thorough description and error analysis of the TOVS water vapor radiance archive, see *Wu et al.* [1993], *Kidwell* [1991], and references therein. In section 4, we use (3) - (5) to infer the distribution of upper, middle, and lower tropospheric relative humidity from the TOVS 6.7, 7.3, and 8.3-μm T_b. For the middle and lower tropospheric channels, all T_b which are not 20 K colder than T_s are adjusted to correct for the surface contribution as described in section 2, where T_s is determined from monthly mean sea-surface temperature analyses [*Reynolds*, 1988]. Hence results for the middle and lower tropospheric channel (which require surface temperature correction) are restricted to ocean surfaces. No adjustments are required for the upper tropospheric channel.

4.1. Geographic Variations

Figure 6a shows a map of the annual-mean upper tropospheric relative humidity (UTH) derived from the TOVS-observed $T_{6.7}$ climatology for the period 1981-1991. The UTH was determined for each day using equation (3) and then averaged over the 11-year period. A timeline of the

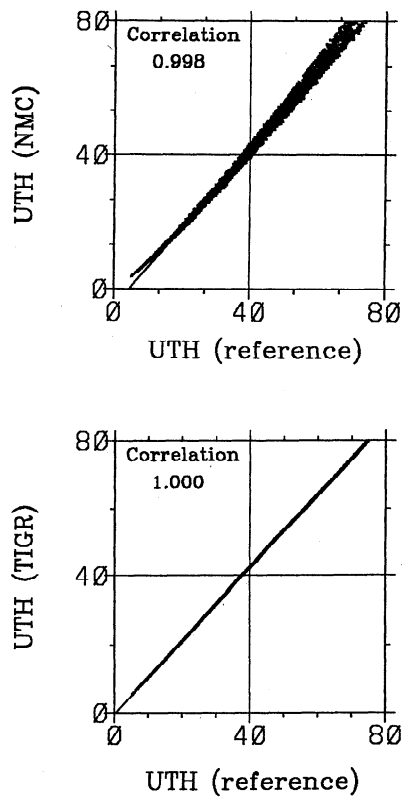

Figure 5. Scatter plot of reference UTH versus that obtained using coefficients from (a) National Meteorological Center (NMC) sample profiles and (b) TOVS initial guess retrieval (TIGR) sample profiles.

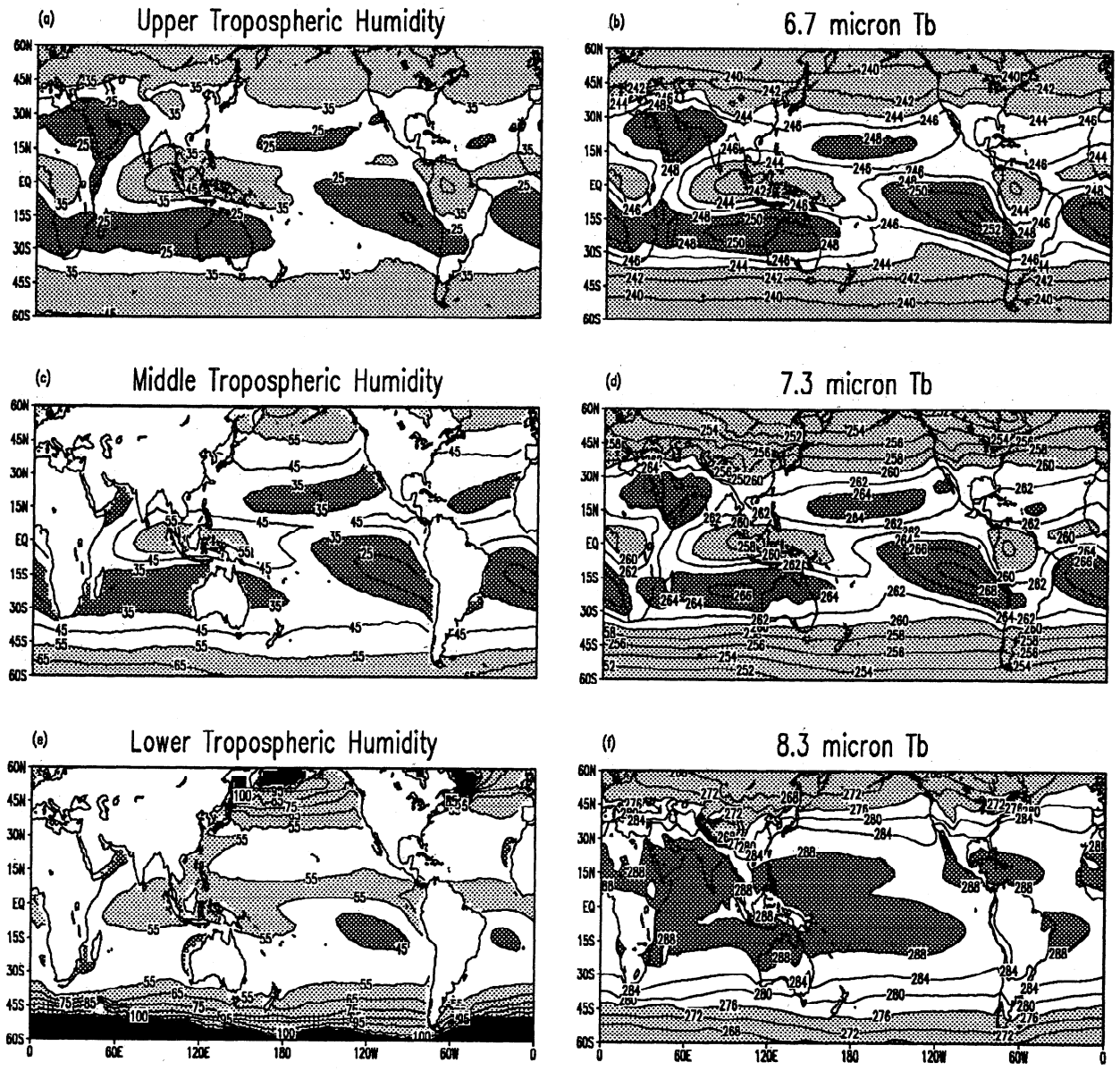

Figure 6. Maps of the annual average (a) upper tropospheric humidity, (b) 6.7-μm brightness temperature, (c) middle tropospheric humidity, (d) 7.3-μm brightness temperature, (e) lower tropospheric humidity, (f) 8.3-μm brightness temperature.

satellite coverage is provided in Table 3. As shown earlier, the UTH is a measure of the relative humidity vertically averaged over a broad layer centered in the upper troposphere (roughly 200-500 mb). Figure 6b depicts the corresponding map of the annual-mean $T_{6.7}$. The close resemblance between the $T_{6.7}$ and UTH fields emphasizes that variation in UTH primarily reflects variations in $T_{6.7}$. Recall that warmer $T_{6.7}$ correspond to a drier atmosphere, while colder $T_{6.7}$ correspond to a moister atmosphere. Both the UTH and $T_{6.7}$ maps clearly show the major features of the Hadley cell circulation with a moist (cold) intertropical convergence zone and a dry (warm) band extending over the subtropics. Moist regions are also observed along the midlatitude storm tracks, over the western Pacific warm pool, and over monsoonal regions of South America and Africa where the relative humidity exceeds 40%. The driest regions are found off the west coasts of South America, Africa, and Australia where the annual mean relative humidity falls below 25%. Recall that the UTH here is defined as the relative humidity with respect to water. To estimate the UTH with respect to ice, one may multiply the values in Figure 6a by ~1.4 (which is the ratio of the saturation vapor pressure with respect to ice over the saturation vapor pressure with respect to water for a typical upper tropospheric temperature of 240 K). Comparable spatial features are observed in radiosonde climatologies of relative humidity above 500 mbar [*Peixoto and Oort*, 1996]. However, the radiosonde and satellite climatologies are not in complete agreement. A detailed comparison of the radiosonde and satellite observations of UTH by [*Soden and Lanzante*, 1996] revealed systematic biases of ~15% relative humidity

Table 3. Dates of Satellite Coverage

Satellite	Period of Coverage
NOAA 6	January 1981 - June 1983
NOAA 7	August 1981 - February 1985
NOAA 8	June 1983 - June 1984
NOAA 9	February 1985 - March 1987
NOAA 10	January 1987 - September 1991
NOAA 11	December 1988 - December 1991

which were shown to result from international differences in radiosonde instrumentation.

Figure 6c shows a map of the annual-mean middle tropospheric humidity (MTH) derived from (4) using the TOVS surface-corrected 7.3-μm brightness temperature climatology (denoted as $T^*_{7.3}$) for the same 11-year period. The results are restricted to ocean surfaces owing to the lack of reliable surface temperatures (needed for the correction) over land. Recall that the MTH corresponds to the relative humidity averaged over a layer extending from roughly 400-800 mbar (see Figure 1). The spatial patterns of the $T_{7.3}$ field (Figure 6d) closely resemble those present in the MTH field. The basic features present in MTH are very similar to those observed for UTH. Most notable is the contrasting dry and moist regions over the tropics, reflecting the upward and downward branches of the Hadley cell, the zonal asymmetry in the tropical Pacific indicative of the Walker circulation, and the moist areas associated with the midlatitude storm tracks. On average, the MTH is slightly greater than the UTH suggesting that the relative humidity tends to decrease with height. The similarity between MTH and UTH indicates that dry (moist) regions in the middle troposphere are strongly correlated with dry (moist) regions in the upper troposphere. The close resemblance between the geographic patterns of relative humidity in the middle and upper troposphere and the tendency for relative humidity to decrease with height are also noted in radiosonde climatologies [*Peixoto and Oort*, 1996].

Figures 6e and 6f depict maps of the annual average lower tropospheric relative humidity (LTH) and $T_{7.3}$. Poleward of 45° latitude little information on LTH is available in the winter hemisphere because the $T_{8.3}$ are rarely 7 K cooler than T_s. Consequently, the sampling of LTH for these latitudes is heavily biased toward summer conditions. In contrast to the upper and middle tropospheric channels, which show a strong similarity between the relative humidity and brightness temperature fields, the distribution of LTH differs noticeably from that of $T_{8.3}$. Indeed, although the LTH, MTH, and UTH all show a broadly similar distribution, the $T_{8.3}$ exhibits a distinctly different spatial pattern from $T_{7.3}$ and $T_{6.7}$. This difference reflects the relatively strong surface contribution to the $T_{8.3}$ hence the spatial pattern of $T_{8.3}$ reflects a combination of the lower tropospheric humidity and surface temperature distributions. Although the primary features noted above are still present, the LTH tends to exhibit less spatial contrast than the relative humidity at higher levels, particularly in the tropics, suggesting that it is not as strongly influenced by large-scale atmospheric motions. Additionally, the relative humidity in the lower troposphere tends to be higher than that in the middle or upper troposphere, again implying that, when averaged over relatively thick layers, relative humidity tends to decrease with height. It is also apparent that the LTH over much of the high-latitude oceans are unrealistically large (i.e., > 100%). These regions are denoted by black shading in Figure 6e. The unrealistically large LTH values are consistent with the contamination of the NESDIS clear-sky 8.3-μm radiance product by low cloud cover in these regions [*Frey et al.*, 1996]. Since cloud tops are generally colder than the underlying surface, cloud contamination results in an underestimate of the clear-sky $T_{8.3}$ and thus an overestimate of the LTH. Similar problems are not apparent for the upper

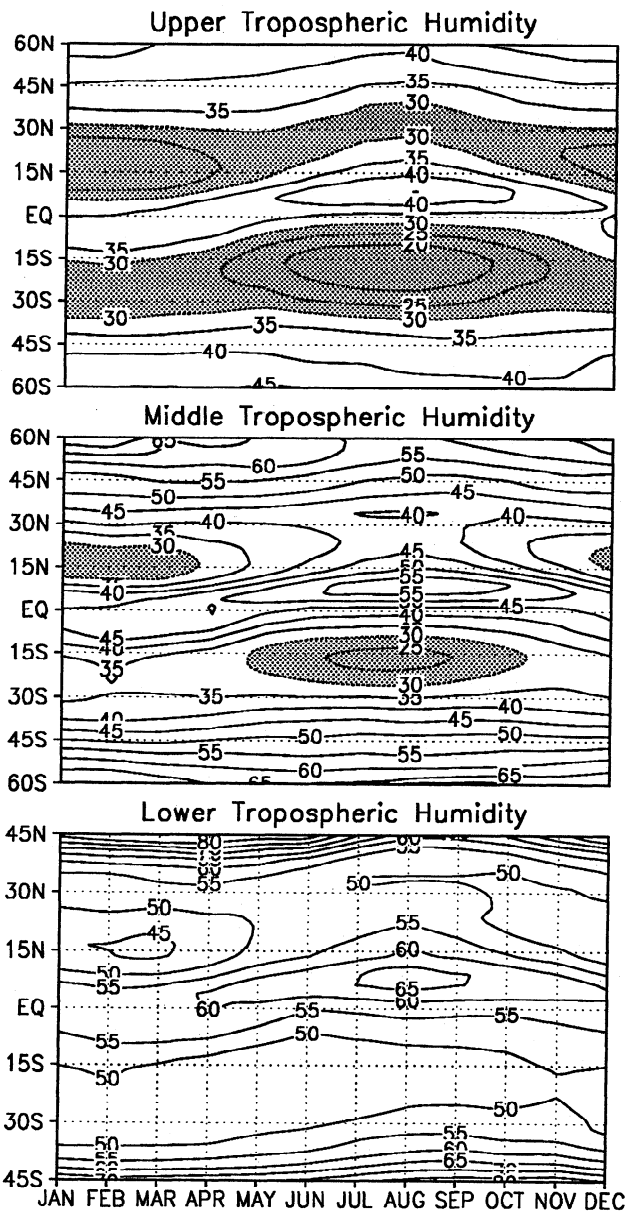

Figure 7. Seasonal variation of (top) upper tropospheric humidity, (middle) middle tropospheric humidit, and (bottom) lower tropospheric humidity. Values less than 30% are shaded.

and middle tropospheric channels because, as shown by Frey et al., the contamination is primarily due to low-level clouds.

4.2. Seasonal Variations

Figure 7 shows the seasonal variation in UTH (top), MTH (middle), and LTH (bottom) averaged over the period 1981-1991. The seasonal variations in relative humidity closely resemble each other in the middle and upper troposphere and emulate the seasonal patterns of variation in the Hadley circulation. Similar, though slightly weaker and less coherent variations are observed in the lower troposphere. The largest changes occur over the tropics where distinct shifts following the seasonal progression of the Intertropical Convergence Zone (ITCZ) are clearly evident. Weaker seasonal variations are noted over the extratropics. For the upper and middle troposphere, maximum relative humidity occurs along the ITCZ from June to September and is associated with a corresponding minimum over the southern hemisphere subtropics during the same period; that is, the wettest period in the tropics coincides with the driest period in the subtropics. A secondary pair of maxima/minima occurs during the southern hemisphere winter, November-February, with the largest relative humidities along the equator and the lowest relative humidities over the northern hemisphere subtropics. Both pairs of minima/maxima typically lag the solstice period by 1.5-2 months. Meridional gradients in relative humidity are smallest during the equinox periods, reflecting a weaker zonal-mean Hadley circulation. Also, note that the southern hemisphere subtropical dry zone is more expansive meridionally and exhibits less seasonal shift than does its counterpart in the northern hemisphere. Radiosonde climatologies display similar seasonal variations in relative humidity [*Peixoto and Oort*, 1996].

To illustrate the zonal asymmetries in the seasonal variation, Figure 8 shows a map of the annual cycle in UTH. For each 2.5° grid box, a fourier analysis was performed on the 11-year time series (1981-1991) of monthly mean data to isolate the annual harmonic and determine its amplitude and phase. The amplitude is given by the length of the arrow in relation to the scale on the lower right. The phase corresponds to the time of maximum UTH and can be determined from the orientation of the arrows with respect to a clock. Arrows pointing toward 1 o'clock correspond to a maximum in January, those toward 2 o'clock correspond to a maximum in February, etc. In most locations, the magnitude of the seasonal variation is much larger than intersatellite calibration differences therefore the results are not sensitive to any radiometric inconsistencies between different satellites. An exception may be along the southern hemisphere midlatitudes where the seasonal variations are small, this may also explain the tendency for less spatial coherence of the phase in this region. The greatest seasonal variations (>10%) are observed over tropical monsoonal regions such as Central America, Brazil, India, and central Africa and exhibit a clear half-year phase difference between regions north and south of the equator. Large seasonal variations also occur over the southeast and northwest quadrants of the tropical Pacific with a similar half-year phase lag. Over the northern extratropics, a distinct land-ocean asymmetry is present. Specifically, the UTH tends to be greatest during winter over North American and Asian continents, while over the Pacific and Atlantic Oceans maximum UTH is observed during summer. Over the southern extratropics, little seasonal variability is observed.

4.3. Interannual Variations

To examine interannual variations in relative humidity, we performed empirical orthogonal function (EOF) analysis on monthly UTH anomalies within the 30°N-30°S tropical belt. The monthly anomalies were determined by subtracting out the 11-year ensemble mean of the annual cycle. Figure 9

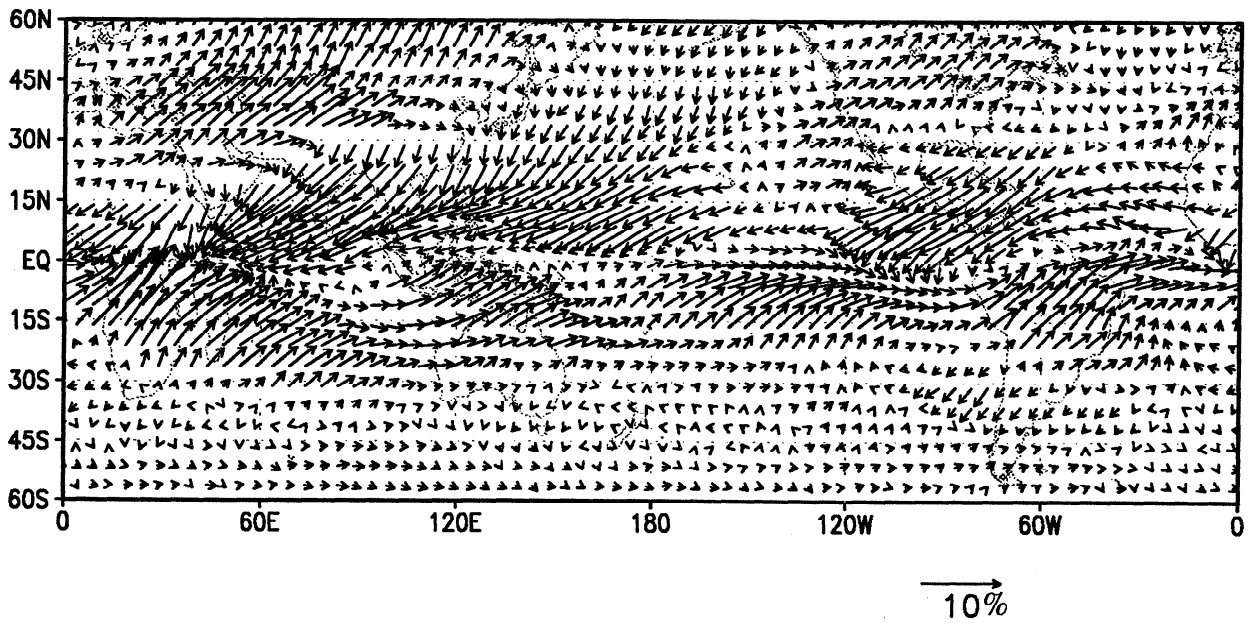

Figure 8. The amplitude and phase of the annual cycle in UTH. The amplitude is given by the length of the arrow in relation to the scaling arrow on the lower right. The phase corresponds to the month of maximum UTH and can be determined from the orientation of the arrows with respect to a clock; 1 o'clock is January, 2 o'clock is February, etc.

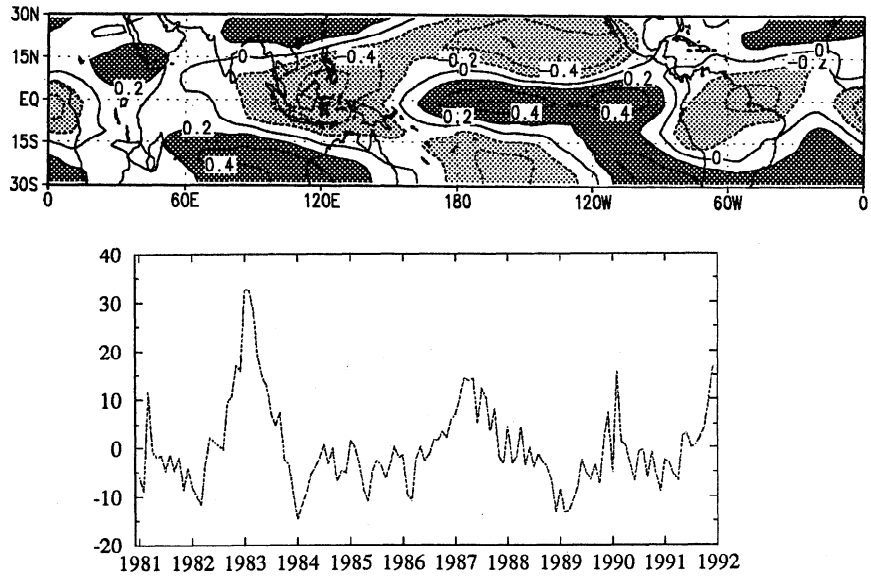

Figure 9. Map of the leading empirical orthogonal function of (top) upper tropospheric relative humidity and (bottom) time series of the corresponding expansion coefficient.

shows the spatial pattern of the leading EOF of the interannual variation of UTH (top) and the corresponding expansion coefficient (bottom) for the period 1981-1991. For brevity only results for UTH are shown as the MTH and LTH patterns exhibit similar features. A similar analysis of the interannual variation in $T_{6.7}$ was recently described by *Bates et al.* [1996]. A notable difference between this study and that of Bates et al., is that the latter used an adjusted $T_{6.7}$ anomaly time series in an attempt to remove intersatellite calibration differences. Although no such adjustment was performed here, the resulting expansion coefficient and EOF pattern are in good agreement with the corresponding quantities determined by Bates et al. Thus for our purpose, the occurrence of slight intersatellite calibration differences does not appear to significantly affect the interpretation.

The first EOF, which explains 11% of the total variance, depicts a pattern of spatial variation commonly associated with the El Nino/ Southern Oscillation (ENSO). This is supported by the expansion coefficients which peak in the early part of 1983 and 1987 and late 1991, all of which correspond to recognized ENSO warm phases. A coherent pattern of UTH anomalies extends throughout the tropical belt. Maximum positive anomalies are located over the central tropical Pacific where a wetter upper troposphere is associated with the eastward shift of convection. Maximum negative anomalies are centered over Indonesia, reflecting a decrease in convective activity over this region during ENSO events and the associated reduction in the Walker circulation. The double lobe apparent in the positive anomaly along the equatorial Pacific is believed to be associated with the late stages of the 1983 ENSO [*Bates et al.*, 1996]. To the north and south of this moist band are negative (dry) anomalies, the strongest of which occurs over the northern subtropics, suggesting an increase in atmospheric subsidence in these regions. An exception to this is the positive anomaly in the southern subtropics off the west coast of South America. An interesting feature of these patterns is that outside the central Pacific the polarity of the anomaly pattern reverses. For example, from 60°W to 120°E negative (dry) anomalies occur over much of the equatorial belt (15°N to 15°S) while positive (moist) anomalies dominate the subtropics (15°-30° N and S). This suggests corresponding changes in the patterns of tropical circulation at these scales during ENSO events.

5. Discussion

Satellite observations of the upwelling radiance in the 6.3-μm water vapor absorption band are used to describe the geographic distribution and temporal variation of relative humidity. The combination of daily, near-global coverage with a coherent archive dating back to 1979 makes TOVS water vapor radiances a valuable source of information on tropospheric water vapor. The water vapor channels, located at 6.7 μm, 7.3 μm, 8.3 μm, are sensitive to the amount of relative humidity integrated over broad layers centered in the upper (200-500 mbar), middle (400-800 mbar), and lower troposphere (700 mbar-surface), respectively. To facilitate the interpretation of the TOVS radiances in terms of a more familiar water vapor quantity, we utilize a simple analytic expression which relates radiance to the vertically averaged relative humidity. This radiance-to-humidity transformation, derived from random strong line theory, indicates that the brightness temperature measures essentially the logarithm of the mean relative humidity averaged over broad layers of the troposphere subject to a straight forward allowance for viewing angle and a minor correction for the mean temperature structure. This simple analytic relation is shown to be consistent with radiative transfer calculations to within approximately 1 K.

The climatological distribution of relative humidity is similar in all three layers, reflecting well-known patterns of the large-scale atmospheric circulation. Peak relative humidities occur along the ITCZ, with minimum values over the subtropics and a second band of maxima over the

midlatitude storm tracks. On average, the UTH is smaller than the MTH and LTH indices, suggesting a general tendency for the relative humidity to decrease with height. Seasonal variations in UTH and MTH are greatest over tropics where they emulate the migration of the Hadley circulation. Weaker seasonal variations are observed over extratropics. Interannual variations demonstrate a clear ENSO signal, with coherent anomalies extending throughout the tropics which reflect changes in the Hadley and Walker circulation.

The TOVS water vapor archive provides valuable information on the distribution and variation in tropospheric water vapor which is suitable for comparison with general circulation models (GCMs) [e.g., *Soden and Bretherton*, 1994; *Schmetz and van de Berg*, 1994; *Salathe et al.*, 1995; *Chen et al.*, 1996]. Although the water vapor radiances are strongly correlated to the layer-mean relative humidities, the most appropriate and consistent method for using satellite observations to evaluate GCMs is to follow a "profile to satellite approach." That is, GCM profiles of temperature and moisture should be inserted into a radiative transfer model to simulate the radiance which would be observed by the satellite under those conditions. One drawback to this approach, however, is that it is often difficult to interpret discrepancies between the observed and GCM-predicted moisture distribution when they are expressed in terms of radiance, rather than other more conventional measures of water vapor (e.g., relative humidity). Fortunately, such insight can be gained by utilizing the simple analytical relationships between radiance and humidity presented here. Namely, discrepancies between the observed and GCM-simulated radiances can be better understood by translating both sets of radiances into relative humidity parameters using (2). Such a procedure is illustrated by *Soden and Bretherton* [1994] and *Chen et al.* [1996]. This approach provides the accuracy of comparing observed with simulated radiances, as well as an easily interpretable measure of tropospheric water vapor. Furthermore, since both the observed and GCM-simulated radiances are treated in a consistent manner, translating the radiances into humidity parameters does not create spurious differences between the two data sets.

References

Bates, J. J., Wu, X., and D. L. Jackson, Interannual variability of upper tropospheric water vapor band brightness temperature, *J. Clim.*, in press, 1996.

Chen, C.-T., E. Roeckner, and B. J. Soden, A comparison of satellite observations and model simulations of column integrated moisture and upper tropospheric humidity, *J. Clim.*, in press, 1996.

Eyre, J. R., A fast radiative transfer model for satellite sounding systems, in *ECMWF Tech. Memo. 176*, Eur. Cent. for Medium-Range Weather Forecasting, Reading England, 1991.

Frey, R. A., S. A. Ackerman, and B. J. Soden, Climate parameters from satellite spectral radiances Part 1: Co-located AVHRR and HIRS/2 observations of the spectral greenhouse parameters, *J. Clim.*, in press, 1996.

Goody, R. M., *Atmospheric Radiation: Theoretical Basis*, Oxford Univ. Press, New York, 1964.

Kidwell, K. B., *NOAA Polar Orbiter User's Guide*, Natl. Oceanic and Atmos. Admin., Silver Spring, Md., 1991.

McMillin, L. M., and C. Dean, Evaluation of a new operational technique for producing clear radiances, *J. Appl. Meteorol.*, *21*, 1005-1014, 1982.

Monine, P., A. Chedin, and N. A. Scott, Automatic classification of air mass type from satellite vertical sounding data: Application to NOAA-7 observations, *Ocean-Air Interactions*, *1*, 95-108, 1987.

Murty, D. G. K., W. L. Smith, H. M. Woolf, and C. M. Hayden, Comparison of radiances observed from satellite and aircraft with calculations using two atmospheric transmittance models, *J. Appl. Opt.*, *32*, 1620-1628, 1993.

Peixoto, J. P. and A. H. Oort, On the climatology of relative humidity in the atmosphere, *J. Clim.*, in press, 1996.

Poc, M., M. M. Roulleau, N. A. Scott and A. Chedin, Quantitative studies of Meteosat water-vapor channel data, *J. Appl. Meteorol.*, *19*, 868-876, 1981.

Reynolds, R. W., A real-time global sea surface temperature analysis, *J. Clim.*, *1*, 75-86, 1988.

Salathe, E. P., D. Chesters, and Y. C. Sud, Evaluation of the upper tropospheric moisture climatology in a GCM using TOVS radiance observations, *J. Clim.*, *8*, 120-132, 1995.

Salathe, E. P. and R. B. Smith, Comparison of 6.7 micron radiances from aircraft soundings and observed from GOES-VAS, *J. Geophys. Res.*, in press, 1996.

Schmetz, J. and L. van de Berg, Upper tropospheric humidity observations from Meteosat compared with short-term forecast fields, *Geophys. Res. Lett.*, *21*, 573-576, 1994.

Soden, B. J. and F. P. Bretherton, Upper tropospheric humidity from the GOES 6.7 μm channel: method and climatology for July 1987, *J. Geophys. Res.*, *98*, 16669-16688, 1993.

Soden, B. J. and F. P. Bretherton, Evaluation of the water vapor distribution in GCMs using satellite observations, *J. Geophys. Res.*, *99*, 1187-1210, 1994.

Soden, B. J. and R. Fu, A satellite analysis of deep convection, upper tropospheric humidity, and the greenhouse effect, *J. Clim.*, *8*, 2333-2351, 1995.

Soden, B. J. and J. R. Lanzante, An assessment of satellite and radiosonde climatologies of upper tropospheric water vapor, *J. Clim.*, in press, 1996.

Wu X., J. J. Bates, and S. J. S. Khalsa, A climatology of water vapor band brightness temperatures from NOAA operational satellite, *J. Clim.*, *6*, 1282-1300, 1993.

F. P. Bretherton, 1225 W. Dayton St., Space Science and Engineering Center, University of Wisconsin, Madison, WI 53706. (e-mail: francisb@ssec.wisc.edu)

B. J. Soden, NOAA Geophysical Fluid Dynamics Laboratory, Princeton University, P.O. Box 308, Princeton, NJ 08542. (e-mail: bjs@gfdl.gov)

(Received April 25, 1995; revised December 5, 1995; accepted December 5, 1995.)